



Cite this: DOI: 10.1039/d5ta03114a

# Thermal stability and electrochemical behavior of commercial polycrystalline and single-crystalline cathodes integrated with cubic $\text{Li}_{6.4}\text{La}_3\text{Zr}_{1.4}\text{Ta}_{0.6}\text{O}_{12}$ for all-solid-state lithium batteries†

Ziting Ma,<sup>a</sup> Grant LaBriola,<sup>a</sup> Karlo Adrian Salazar,<sup>a</sup> Chunting Chris Mi <sup>b</sup> and Lingping Kong <sup>\*ac</sup>

All-solid-state lithium batteries (ASSLBs) have emerged as promising next-generation energy storage systems, offering enhanced safety and higher energy density compared to conventional Li-ion batteries. However, their practical performance remains limited by interfacial instabilities. In this work, we systematically investigate the interfacial reactions and secondary phase formation between garnet-type cubic  $\text{Li}_{6.4}\text{La}_3\text{Zr}_{1.4}\text{Ta}_{0.6}\text{O}_{12}$  (LLZTO) and a variety of commercial cathode materials, including polycrystalline  $\text{LiNi}_{0.5}\text{Mn}_{1.5}\text{O}_4$  (pc-LNMO),  $\text{LiCoO}_2$  (pc-LCO),  $\text{LiNi}_{1-x-y}\text{Mn}_x\text{Co}_y\text{O}_2$  (pc-NMC811, 631, 532, 111), and single-crystalline NMC631 (sc-NMC631). Structural analyses reveal that interfacial phase evolution is highly dependent on cathode composition, crystal structure, and sintering temperature. Among all compositions studied, sc-NMC631 exhibits superior thermal compatibility with LLZTO, maintaining phase integrity up to 1000 °C. In contrast, polycrystalline cathodes undergo distinct interfacial degradation:  $\text{La}_2\text{Zr}_2\text{O}_7$  and  $\text{LaCoO}_3$  form at 700 °C in pc-LCO + LLZTO, while  $\text{Li}_2\text{MnO}_3$  and  $\text{La}_2\text{Zr}_2\text{O}_7$  emerge as early as 400 °C in pc-LNMO + LLZTO. In pc-NMC + LLZTO composites,  $\text{LaMO}_3$ -type (M: Ni, Mn, Co) phases are consistently observed. Additionally,  $\text{La}_2(\text{Ni}_{0.5}\text{Li}_{0.5})\text{O}_4$  phase is present in these Ni-rich compositions and  $\text{Li}_2\text{MnO}_3$  is in the Ni-lean NMC111. Electrochemical studies reveal a 63% capacity loss in pc-NMC631 + LLZTO-900, primarily due to resistive interfacial phases and poor solid–solid contact that impede Li-ion transport. In comparison, sc-NMC631 + LLZTO-900 demonstrates a lower capacity loss of 48%, attributed to enhanced interfacial stability over its polycrystalline counterpart. However, the remaining capacity loss is likely due to misaligned Li-ion transport pathways across the rigid solid–solid interface. These results highlight the critical role of cathode selection and interface engineering in garnet-based ASSLBs and establish sc-NMC631 as a promising candidate for high-performance composite cathodes.

Received 20th April 2025

Accepted 13th July 2025

DOI: 10.1039/d5ta03114a

rsc.li/materials-a

## 1. Introduction

Global energy consumption is projected to increase by approximately 50% by 2050, driving the demand for sustainable and efficient energy storage technologies to meet future energy needs. Concurrently, achieving net-zero or even negative carbon emissions is essential for ensuring climate stability. However, the existing energy storage systems, such as state-of-the-art Li-ion batteries (LiBs) employing liquid or gel-polymer electrolytes face limitations in safety, energy density, and

environmental sustainability, rendering them insufficient to meet future demands. All-solid-state lithium batteries (ASSLBs) have emerged as a promising alternative, offering enhanced safety, higher energy density, and prolonged cycle life through the use of non-flammable solid-state electrolytes (SEs) and high-capacity lithium-metal (Li-metal) anodes.<sup>1,2</sup> Within ASSLBs, the selection of suitable SEs plays a critical role to realizing these advantages. Key requirements for SEs include high ionic conductivity, wide electrochemical stability window, thermal and chemical robustness, and strong electro-chemo-mechanical compatibility with both cathode materials and Li-metal anodes.<sup>2,3</sup>

Among the various SE candidates, garnet-type cubic  $\text{Li}_7\text{La}_3\text{Zr}_2\text{O}_{12}$  (LLZO) has garnered significant attention due to its favorable properties, including high ionic conductivity (up to 0.5  $\text{mS cm}^{-1}$  at 25 °C),<sup>4</sup> a wide electrochemical stability window (0–5 V vs.  $\text{Li/Li}^+$ ), and chemical compatibility with Li-metal.<sup>5</sup>

<sup>a</sup>Department of Mechanical Engineering, San Diego State University, CA, 92182, USA. E-mail: lkong@sdsu.edu

<sup>b</sup>Department of Electrical and Computer Engineering, San Diego State University, CA, 92182, USA

<sup>c</sup>SDSU Research Foundation, San Diego, CA, 92182, USA

† Electronic supplementary information (ESI) available. See DOI: <https://doi.org/10.1039/d5ta03114a>

Enhanced performance has been achieved through supervalent cation doping, such as substituting Ta<sup>5+</sup> or Nb<sup>5+</sup> at the Zr<sup>4+</sup>-site, Al<sup>3+</sup> or Ga<sup>3+</sup> at the Li<sup>+</sup>-site, will not only stabilize the cubic phase but also increase ionic conductivity up to 1 mS cm<sup>-1</sup> (e.g., Li<sub>6.4</sub>La<sub>3</sub>Zr<sub>1.4</sub>Ta<sub>0.6</sub>O<sub>12</sub>, LLZTO).<sup>5,6</sup> Despite these advantages, one of the primary challenges in LLZTO-based ASSLBs is the interfacial instability between LLZTO and the cathode materials. While considerable progress has been made in reducing interfacial resistance at the LLZTO–Li metal interface,<sup>7,8</sup> the LLZTO–cathode interface remains problematic due to high interfacial resistance, chemical incompatibility, and gradually electrochemical and mechanical degradation during cycling, which collectively hinder battery performance.<sup>9,10</sup>

To enhance interfacial contact and facilitate charge transport, high-temperature sintering is commonly employed to fabricate cathode + LLZTO composite structures. However, this approach often leads to cation interdiffusion and undesirable

side reactions, resulting in the formation of ionically and electronically insulating secondary phases that degrade battery performance.<sup>2,10</sup> Fig. 1 summarizes the sintering conditions, identified secondary phases, and characterization methods used to investigate cathode + LLZTO composites. The formation of interfacial phases is highly dependent on cathode composition and processing parameters. For instance, sintering LiCoO<sub>2</sub> (LCO) with LLZTO at 700 °C has been reported to result in LaCoO<sub>3</sub> formation, a known ionic and electronic insulator at the interface.<sup>11</sup> In contrast, other reports suggest that LCO remains interfacial stability with LLZTO at the temperature up to 900 °C.<sup>12,13</sup> In thin-film configurations, element interdiffusion has been observed even at relatively lower processing temperatures (300–700 °C), likely due to their high surface-to-volume ratios,<sup>14,15</sup> as illustrated in Fig. 1a.

The chemical composition of high-voltage spinel cathodes like LiNi<sub>0.5</sub>Mn<sub>1.5</sub>O<sub>4</sub> (LNMO, in Fig. 1b) and ternary layered oxide

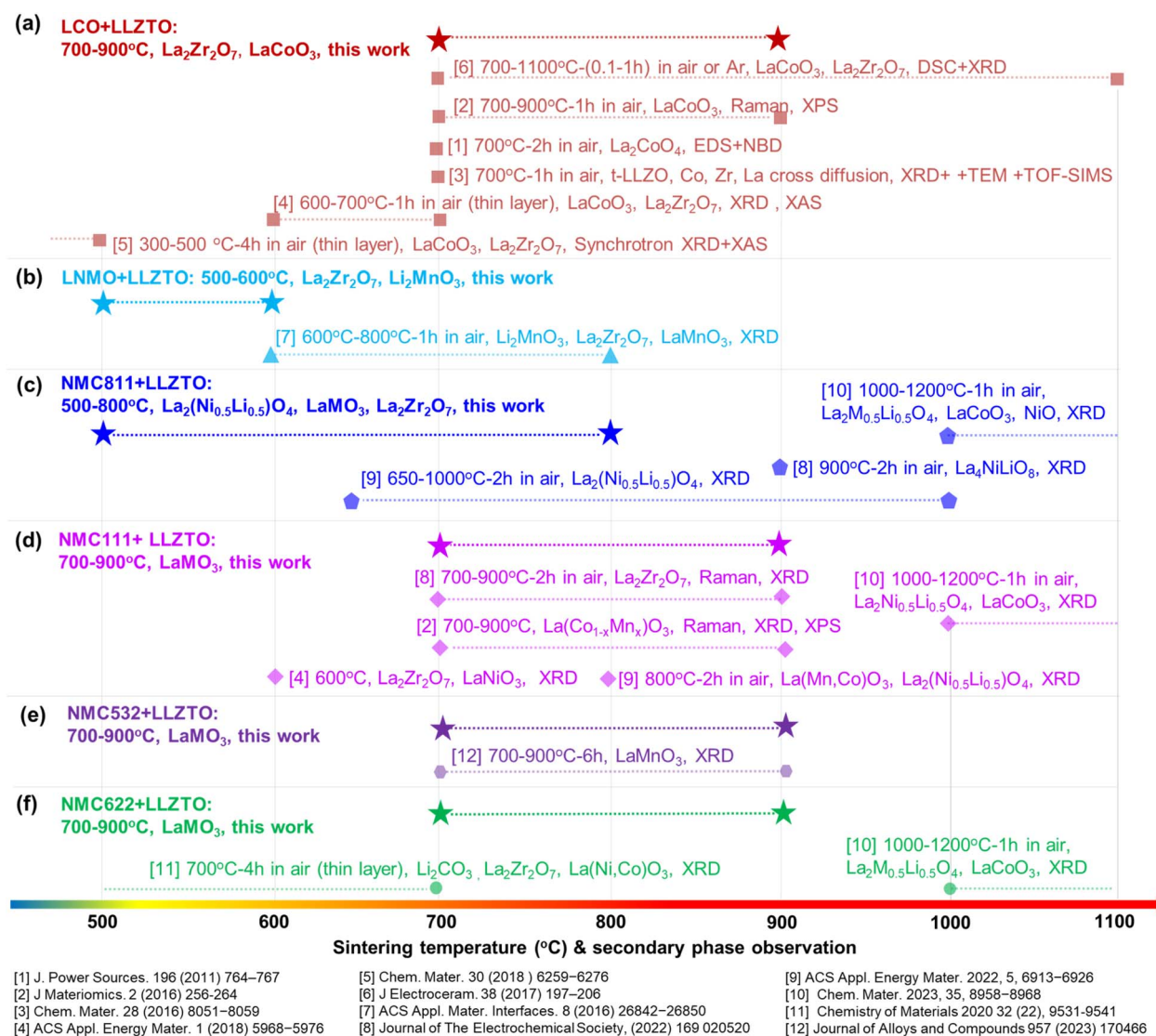


Fig. 1 Summary of sintering conditions for cathode material + garnet-type solid electrolyte composite, associated secondary phase formation, and the characterization techniques employed for their analysis.

cathodes, such as  $\text{LiNi}_{1-x-y}\text{Mn}_x\text{Co}_y\text{O}_2$  (NMC, in Fig. 1c–f), plays a critical role in determining their thermal compatibility with garnet-type SEs.<sup>9,16</sup> For example, Ni-rich NMC811 undergoes interfacial reactions with LLZTO, forming  $\text{La}_2(\text{Ni}_{0.5}\text{Li}_{0.5})\text{O}_4$  at 650 °C, with the amount increasing to 2 wt% at 800 °C and more extensive phase formation observed at 900 °C.<sup>12,17</sup> Reducing the Ni content to 60% in NMC622 improves thermal stability up to 900 °C; however, secondary phases such as  $\text{LaCoO}_3$  and  $\text{La}_2\text{M}_{0.5}\text{Li}_{0.5}\text{O}_4$  (M: Ni, Mn, Co) still appear at 1000 °C and above.<sup>18</sup> In contrast, Ni-lean and Mn-rich compositions like NMC111 begin forming a Li-deficient phase,  $\text{La}_2\text{Zr}_2\text{O}_7$ , at 700 °C,<sup>12</sup> with  $\text{LaCoMnO}_3$  appearing at 800 °C (ref. 17) and  $\text{LaMO}_3$ -type phases (M: Ni, Mn, Co) observed at 900 °C.<sup>11</sup> Even minimal formation of these secondary phases can significantly degrade electrochemical performance; for example, the presence of 1.0 wt%  $\text{La}_2\text{Zr}_2\text{O}_7$  in an NMC111 + LLZTO composite was shown to reduce the active material capacity to 60% of its original value.<sup>12</sup> Additionally, the sintering atmosphere also influences the phase evolution. In oxygen-free environments, NMC532 undergoes structural transformations from a layered structure to spinel and rock-salt phases, while these transitions are suppressed when sintered in synthetic air.<sup>19</sup>

Beyond composition, the crystallographic structure of cathode materials also has impacts on electrochemical performance of ASSLBs.<sup>20</sup> Polycrystalline cathode materials often suffer from limited cycle life due to mechanical failure. During electrochemical cycling, volumetric changes within secondary particles generate internal strain and stress, ultimately leading to microcracking and structural breakdown.<sup>21,22</sup> This issue is particularly pronounced in ASSLBs, where the rigid solid–solid interfaces between cathode materials and solid electrolytes inhibits the accommodation of mechanical deformation. To mitigate these challenges, single-crystalline cathode particles have been developed, demonstrating enhanced mechanical integrity in both liquid electrolyte systems and soft solid-state electrolytes such as halides and sulfides.<sup>20,23</sup> However, the electrochemical behavior and mechanical durability of single-crystalline cathodes in oxide-based ASSLBs are still under investigation. A detailed understanding of their thermal compatibility with garnet-type SEs and the impact of crystallographic structure on interfacial Li-ion transport is essential for further advancement.

In this study, we systematically investigated the thermochemical stability and secondary phase formation resulting from high-temperature sintering of cubic  $\text{Li}_{6.4}\text{La}_3\text{Zr}_{1.4}\text{Ta}_{0.6}\text{O}_{12}$  (LLZTO) with various commercial cathode materials, including polycrystalline  $\text{LiCoO}_2$  (LCO),  $\text{LiNi}_{0.5}\text{Mn}_{1.5}\text{O}_4$  (LNMO), and a range of NMC compositions:  $\text{LiNi}_{0.8}\text{Mn}_{0.1}\text{Co}_{0.1}\text{O}_2$  (NMC811),  $\text{LiNi}_{0.67}\text{Mn}_{0.28}\text{Co}_{0.05}\text{O}_2$  (NMC631),  $\text{LiNi}_{0.5}\text{Mn}_{0.3}\text{Co}_{0.2}\text{O}_2$  (NMC532), and  $\text{Li}_{1.05}\text{Ni}_{0.33}\text{Mn}_{0.33}\text{Co}_{0.33}\text{O}_2$  (NMC111), along with single-crystalline  $\text{LiNi}_{0.6}\text{Mn}_{0.3}\text{Co}_{0.1}\text{O}_2$  (sc-NMC631). Using a comprehensive suite of characterization techniques, we examined the formation of secondary phases under standardized sintering protocols, enabling consistent and reproducible analysis. Furthermore, the electrochemical properties of single-crystalline and polycrystalline NMC + LLZTO composites were evaluated following high-temperature sintering, to assess the

influence of particle morphology and interphase. These findings provide critical insights into the design of chemically and structurally compatible cathode materials for garnet-based ASSLBs and establish benchmarks to guide the development of durable and high-performance all-solid-state energy storage systems.

## 2. Experimental

### 2.1 Cathode composite preparation

Commercial powders of cubic  $\text{Li}_{6.4}\text{La}_3\text{Zr}_{1.4}\text{Ta}_{0.6}\text{O}_{12}$  (LLZTO), polycrystalline  $\text{LiCoO}_2$  (pc-LCO),  $\text{LiNi}_{0.5}\text{Mn}_{1.5}\text{O}_4$  (pc-LNMO),  $\text{LiNi}_{0.8}\text{Mn}_{0.1}\text{Co}_{0.1}\text{O}_2$  (pc-NMC811),  $\text{LiNi}_{0.67}\text{Mn}_{0.28}\text{Co}_{0.05}\text{O}_2$  (pc-NMC631),  $\text{LiNi}_{0.5}\text{Mn}_{0.3}\text{Co}_{0.2}\text{O}_2$  (pc-NMC532) and  $\text{Li}_{1.05}\text{Ni}_{0.33}\text{Mn}_{0.33}\text{Co}_{0.33}\text{O}_2$  (pc-NMC111), and single-crystalline  $\text{LiNi}_{0.6}\text{Mn}_{0.3}\text{Co}_{0.1}\text{O}_2$  (sc-NMC631), along with Super C65 carbon black, were obtained from MSE Supplies®. Polyvinylidene fluoride (purity > 99.5%, PVDF) was purchased from MTI Corporation, and 1.0 M  $\text{LiPF}_6$  in EC/DMC/DEC (vol% 1 : 1 : 1) (lithium hexafluorophosphate solution in ethylene carbonate, dimethyl carbonate and diethyl carbonate) and 1-methyl-2-pyrrolidinone (NMP) (purity > 99.5%) were sourced from MilliporeSigma®. Material morphologies and microstructural details are provided in Table S1 and Fig. S1.† All materials were used as received. This study focuses on a systematic evaluation of the thermochemical stability of commercially available cathode materials integrated with LLZTO, as well as their electrochemical performance after high-temperature sintering. The effects of cathode material impurities (e.g. differences between suppliers), particle size distribution, and volume ratios between the cathode material and solid electrolyte were not considered.

To ensure consistent evaluation of thermochemical and electrochemical properties, all composites were processed under identical conditions, varying only in sintering temperature. Cathode and LLZTO powders were manually mixed (1 : 1 wt ratio) for 20 minutes in an Ar-filled glovebox using a mortar and pestle to deagglomerate particles and achieve a homogeneous mixture and avoid moisture. Approximately 300 mg of the mixture was pressed into 10 mm diameter green pellets under 100 MPa for 5 minutes to ensure intimate particle contact. Green pellets were sintered in lidded magnesium oxide ( $\text{MgO}$ ) crucibles at selected temperatures for 2 hours in an  $\text{O}_2$  atmosphere, with a ramp rate of  $10\text{ °C min}^{-1}$ , followed by natural cooling. Sintering temperatures were chosen based on thermogravimetric analysis (TGA), and 2 hours was found sufficient for forming solid–solid interfaces. The resulting pellets were labelled as “cathode + LLZTO-*T*” (e.g., pc-LCO + LLZTO-800) and stored in an Ar-filled glovebox for subsequent use.

### 2.2 Characterization

Thermogravimetric analysis (TGA) were conducted using a TA Instruments Q600 SDT, with a heating rate of  $5\text{ °C min}^{-1}$  up to 1100 °C in synthetic air, pure oxygen (21%) and pure nitrogen (79%). The morphology and nanostructure of the materials was characterized using a FEI Quanta 450 FEG Scanning Electron Microscope (SEM) and JEOL JEM-2800 TEM. Raman spectra

were collected using a Thermo Scientific DXR3 Raman microscope equipped with a 532 nm laser and a grating of 900 lines per mm. The laser power was set to 5 mW to prevent laser-induced sample damage. Background subtraction and spectral normalization were applied. X-ray diffraction (XRD) was performed on a Rigaku MiniFlex 600-C using Cu-K $\alpha$  radiation source, over a  $2\theta$  range of 10–80°, with a scan speed of 3.0° min<sup>-1</sup> and a step size of 0.01°. The raw data were analyzed using SmartLab Studio II.

### 2.3 Electrode preparation, cell assembly, and electrochemical testing

The electrochemical performance of the sintered cathode composites was evaluated in slurry-coated electrodes assembled in coin cells using a liquid electrolyte. Cathode composite pellets were manually crushed and ground into power in an Ar-filled glovebox before electrode fabrication. Slurries were prepared by mixing composite powder, PVDF binder, and Super C65 (85 : 7.5 : 7.5 wt%) in NMP followed by 2 hours magnetic stirring. The homogeneous slurry was cast onto Al foil (purity  $\geq$  99.3%, MTI Corporation) using a mini tape-casting coater (MSK-AFA-HC100, MTI Corporation), then dried overnight at 100 °C under a vacuum of 30" Hg, followed by punching into 14 mm electrode discs. Cathode active material loading was *ca.*  $\sim$ 1.8 mg cm<sup>-2</sup>.

CR2032 coin cells were assembled in an Ar-filled glovebox (LC Technology Solutions, Inc.) with a water/oxygen content < 1 ppm, using Li-metal discs (15.6 mm diameter, 460  $\mu$ m

thickness; Guangdong Canrd New Energy Technology, China) as reference and counter electrodes, Celgard-2500 (Celgard) as the separator, and 1.0 M LiPF<sub>6</sub> in EC/DMC/DEC (vol% 1 : 1 : 1) as the liquid electrolyte. As a control, the electrochemical performance of pc-NMC631 and sc-NMC631 cathode materials without LLZTO was evaluated in a liquid electrolyte system and labeled as pc-NMC631-LE and sc-NMC-631-LE, respectively.

Electrochemical tests were conducted at  $\sim$ 22 °C using a VSP potentiostat (Biologic, USA). CV test was carried out at a scan rate of 0.1 mV s<sup>-1</sup> and electrochemical impedance spectroscopy (EIS) was recorded using an amplitude of 10 mV over 500 kHz to 50 mHz. Rate performance was evaluated on a LANDT battery tester (CT2001A, Landt Instruments, USA). The current density and specific capacity were calculated based on the mass of the cathode active materials, and the working potential was set between 3.0–4.5 V (*vs.* Li/Li<sup>+</sup>).

## 3. Results and discussion

The thermal stability of cathode materials plays a critical role in evaluating their compatibility with cubic Li<sub>6.4</sub>La<sub>3</sub>Zr<sub>1.4</sub>Ta<sub>0.6</sub>O<sub>12</sub> (LLZTO) for all-solid-state lithium batteries (ASSLBs). Thermogravimetric analysis (TGA) was employed to study the thermal behavior of pure polycrystalline and single-crystalline cathodes, as shown in Fig. 2a. Among them, pc-LCO demonstrated the highest thermal stability, maintaining nearly constant weight up to 1050 °C, with slight weight loss at higher temperatures attributed to Li volatilization and phase

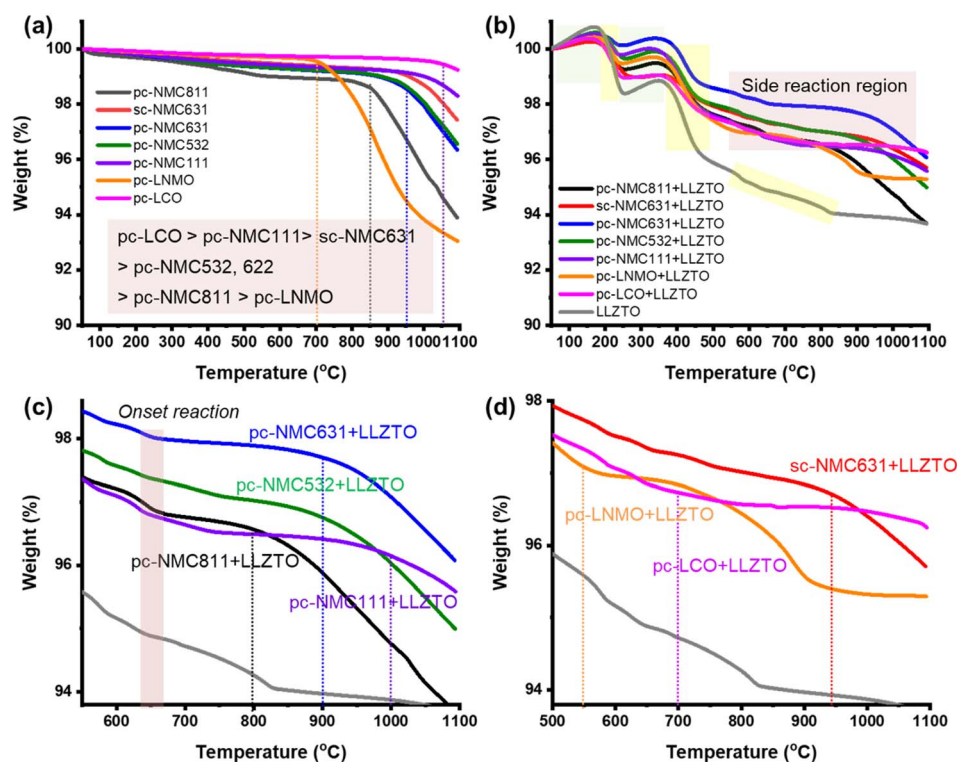


Fig. 2 (a) Thermal stability of cathode materials and (b) thermochemical compatibility with LLZTO. Zoomed-in TGA profiles of (c) pc-NMC + LLZTO and (d) pc-LNMO, pc-LCO, sc-NMC631 + LLZTO composites.

transitions.<sup>24</sup> In contrast, pc-LNMO began to decompose around 700 °C, likely due to oxygen evolution and disproportionation reactions that result in Ni deficiency in the LNMO phase and the formation of secondary  $\text{Li}_2\text{Ni}_{1-x}\text{O}$  phases.<sup>25</sup> For polycrystalline NMC materials, the decomposition temperature was inversely related to Ni content, consistent with prior reports attributing this trend to oxygen release and structural phase transitions.<sup>26</sup> Among these, pc-NMC111 showed higher stability, followed by pc-NMC631, 532, with pc-NMC811 being the least stable. The sc-NMC631 showed better thermal stability than its polycrystalline counterpart. Overall, the order of thermal stability was: pc-LCO > pc-NMC111 > sc-NMC631 > pc-NMC631  $\approx$  pc-NMC532 > pc-NMC811 > pc-LNMO. LLZTO's purity is highly sensitive to moisture due to Li/proton exchange and LiOH formation induced surface  $\text{Li}_2\text{CO}_3$  contamination. As shown in Fig. 2b, LLZTO exhibited three main weight loss steps at 200–250 °C, 350–500 °C, and 550–800 °C, with a total weight loss of  $\sim 6$  wt%. These losses are attributed to the removal of  $\text{H}_2\text{O}$  and  $\text{CO}_2$  through Li/proton exchange mechanism,<sup>27</sup> as further confirmed by Raman spectroscopy (Fig. S2a†). Exposure of garnet-type solid electrolytes to ambient moisture facilitates Li/proton exchange and leads to surface  $\text{Li}_2\text{CO}_3$  contamination.

Thermochemical reactions between cathode materials and LLZTO were investigated using 1 : 1 wt% composite powders. All composites exhibited similar thermal behavior up to 550 °C (Fig. 2b), after that decomposition behaviors diverged, indicating the onset temperatures of side reactions vary among different cathode materials. As zoomed in Fig. 2c, pc-NMC + LLZTO composites began to degrade at different temperatures depending on cathode composition:  $\sim 800$  °C for pc-NMC811, 900 °C for pc-NMC631, 532, and 1000 °C for pc-NMC111,

indicating that the thermal compatibility of pc-NMC with LLZTO decreased with increasing Ni content.<sup>28</sup> Interestingly, sc-NMC631 + LLZTO exhibited better thermal compatibility than pc-NMC631 + LLZTO, despite their similar stoichiometry (Fig. 2d), likely due to the lower defect density in the single-crystal structure. In pc-LCO + LLZTO composite showed a notable mass loss at  $\sim 700$  °C, which was not observed in the individual components, indicating interfacial reactivity. The pc-LNMO + LLZTO composites had the lowest onset temperature for side reactions, around 550 °C, underscoring its poor thermal compatibility with LLZTO. The formation of secondary phases in these composites was further investigated through X-Ray diffraction (XRD) and Raman spectroscopy analyses. These findings highlight the critical need to tailor sintering conditions for cathode + LLZTO composites to minimize interfacial reactions and preserve electrochemical performance.

XRD patterns and Raman spectra of pc-LCO + LLZTO composites sintered at various temperatures are shown in Fig. 3a and b. Phase changes began to occur at 700 °C, as indicated by the appearance of a new phase with a diffraction peak centered at  $27^\circ$  and a Raman peak at  $304\text{ cm}^{-1}$ , corresponding to a Li-deficient  $\text{La}_2\text{Zr}_2\text{O}_7$  phase (labelled with  $\blacktriangledown$ ), which has poor ionic conductivity.<sup>2</sup> This suggests lithium diffusion from LLZTO into LCO, facilitating the formation of the  $\text{La}_2\text{Zr}_2\text{O}_7$  phase. A new Raman peak at  $683.4\text{ cm}^{-1}$  was also detected, attributed to  $\text{LaCoO}_3$ , based on the symmetric O–M–O stretching vibration mode of  $[\text{MO}_6]$  octahedra in rhombohedral  $\text{LaMO}_3$  (M: Co) (labelled with  $\blacklozenge$ ).<sup>29,30</sup> At 900 °C, the intensity of  $\text{LaCoO}_3$  peaks increased, while the  $\text{La}_2\text{Zr}_2\text{O}_7$  peak decreased. Rietveld refinement estimates the total fraction of  $\text{LaCoO}_3$  and  $\text{La}_2\text{Zr}_2\text{O}_7$  phases to be 3.1 wt%. In contrast, for the composite

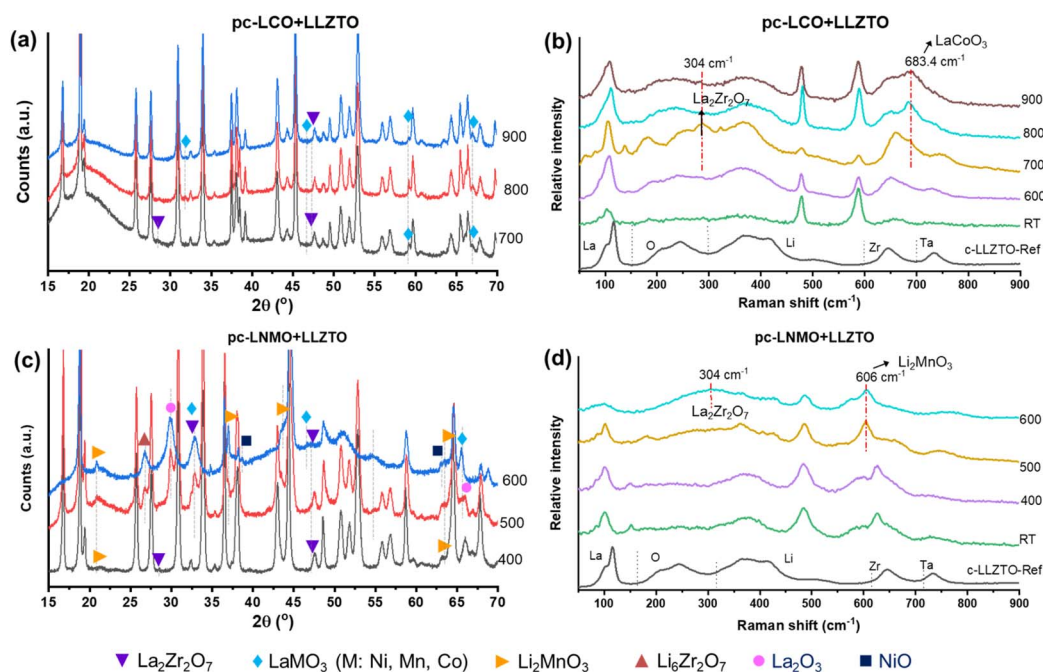


Fig. 3 XRD patterns and Raman spectra of (a and b) pc-LCO + LLZTO and (c and d) pc-LNMO + LLZTO composites sintered at various temperatures in an  $\text{O}_2$  atmosphere for 2 hours. Raman spectra of pure LLZTO are included for reference.

sintered at 600 °C, no significant changes were observed in Raman spectra (Fig. 3b and S4†), confirming that secondary phase formation begins at 700 °C. To mitigate element interdiffusion during high-temperature processing, incorporating a protective buffer layer such as  $\text{Li}_3\text{BO}_3$  is recommended.<sup>9</sup>

For pc-LNMO + LLZTO composites sintered at 600, 500, 400 °C, the corresponding XRD patterns and Raman spectra in Fig. 3c and d, revealing phase evolution from 400 to 600 °C. At 400 °C, a Li-rich monoclinic  $\text{Li}_2\text{MnO}_3$  phase (labelled with ►) appeared with XRD peaks centered at 20.7° and 63.6°, while

a Li-deficient phase  $\text{La}_2\text{Zr}_2\text{O}_7$  (▼) emerged with XRD peaks located at 28.4° and 47.3°. These changes are attributed to lithium diffusion from LLZTO to LNMO, forming both a Li-rich phase and Li-deficient phase. The insulating  $\text{La}_2\text{Zr}_2\text{O}_7$  phase can block charge transfer at the interface, while  $\text{Li}_2\text{MnO}_3$  has limited capacity as a cathode material.<sup>16</sup> At 600 °C, the amount of  $\text{Li}_2\text{MnO}_3$  and  $\text{La}_2\text{Zr}_2\text{O}_7$  increased, and additional phases including  $\text{LaMO}_3$  (M: Mn) (◆),  $\text{Li}_6\text{Zr}_2\text{O}_7$  (▲),  $\text{La}_2\text{O}_3$  (●), and NiO (■) appeared, with LLZTO no longer detectable. These results demonstrate that side reactions between LNMO and LLZTO

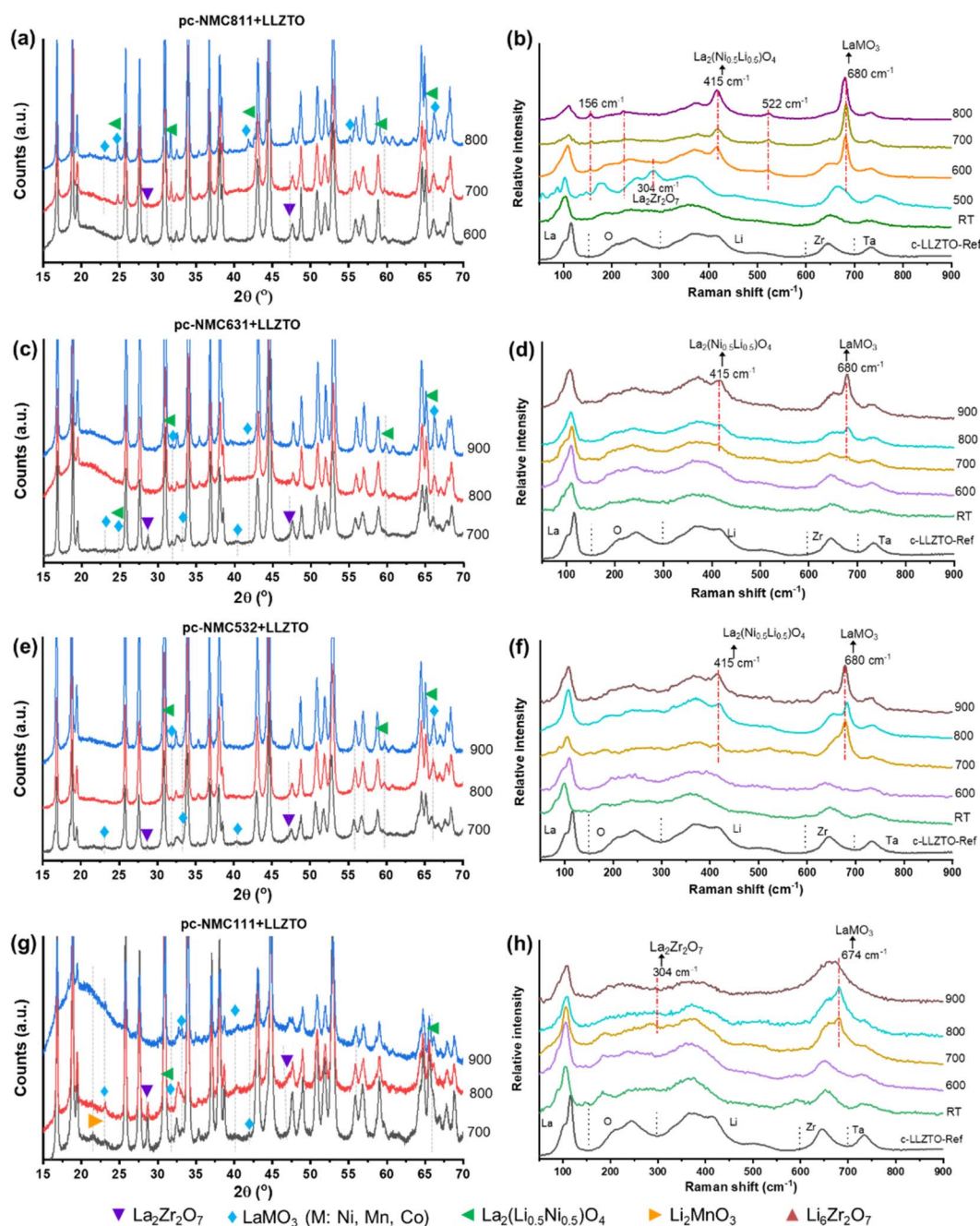


Fig. 4 XRD patterns and Raman spectra of (a and b) pc-NMC811 + LLZTO, (c and d) pc-NMC631 + LLZTO, (e and f) pc-NMC532 + LLZTO, and (g and h) pc-NMC111 + LLZTO composites sintered at various temperatures in an  $\text{O}_2$  atmosphere for 2 hours. Raman spectra of cubic LLZTO are included for reference.

begin at temperatures as low as 400 °C, with severe degradation of cubic LLZTO structure at 600 °C. The impact of heat-treatment on LNMO structural stability is further discussed in Fig. S5.†

The effect of NMC composition on thermochemical compatibility with LLZTO was systematically investigated, and the corresponding XRD patterns and Raman spectra are presented in Fig. 4. XRD patterns and Raman spectra of pure NMC cathode materials are provided in Fig. S6.† All pc-NMC + LLZTO composites showed evidence of cation interdiffusion with new peaks appearing at elevated sintering temperatures. For pc-NMC811 + LLZTO composites (Fig. 4a and b), a new Raman peak at 304 cm<sup>-1</sup> was observed at 500 °C, corresponding to La<sub>2</sub>Zr<sub>2</sub>O<sub>7</sub> formation. As the sintering temperature increased from 600 °C to 800 °C, additional new Raman peaks emerged at 156, 415, 522, and 680 cm<sup>-1</sup>, indicating the formation of La<sub>2</sub>(Ni<sub>0.5</sub>Li<sub>0.5</sub>)O<sub>4</sub> (labelled with ◀<sup>31</sup>) and a Li-deficient perovskite phase, LaMO<sub>3</sub> (M: Ni, Co, Mn) (labelled with ♦).<sup>11,17</sup> XRD confirmed the formation LaMO<sub>3</sub> at 23.0° and 24.8°, La<sub>2</sub>(Ni<sub>0.5</sub>Li<sub>0.5</sub>)O<sub>4</sub> at 24.6° and 33.8°. The total fraction of secondary phases in pc-NMC811 + LLZTO-800 was estimated to be 2.0 wt% based on Rietveld refinement. La<sub>2</sub>Zr<sub>2</sub>O<sub>7</sub> phase could not be detected at 800 °C.

For pc-NMC631, 532 + LLZTO composites, they exhibited similar thermal compatibility when integrated with LLZTO, as shown in Fig. 4c–f. The primary phases remained stable up to 600 °C, with no clear evidence of secondary phase formation. At 700 °C, XRD patterns of both composites showed La<sub>2</sub>Zr<sub>2</sub>O<sub>7</sub>, LaMO<sub>3</sub>, and La<sub>2</sub>(Ni<sub>0.5</sub>Li<sub>0.5</sub>)O<sub>4</sub> phases. The La<sub>2</sub>Zr<sub>2</sub>O<sub>7</sub> intensity decreased at 800 °C and was undetectable at 900 °C, while LaMO<sub>3</sub> and La<sub>2</sub>(Ni<sub>0.5</sub>Li<sub>0.5</sub>)O<sub>4</sub> intensities increased. Raman spectra confirmed these phase changes, with the peaks at

680 cm<sup>-1</sup> and 415 cm<sup>-1</sup> corresponding to LaMO<sub>3</sub> and La<sub>2</sub>(Ni<sub>0.5</sub>Li<sub>0.5</sub>)O<sub>4</sub>, respectively. For pc-NMC111 + LLZTO, which has the lowest Ni content and a Mn-rich composition, phase stability was maintained up to 600 °C (Fig. 4g and h). At 700 °C, Li<sub>2</sub>MnO<sub>3</sub>, La<sub>2</sub>Zr<sub>2</sub>O<sub>7</sub>, and LaMO<sub>3</sub> phases were observed, and the LaMO<sub>3</sub> peak intensity increased at higher sintering temperatures. However, La<sub>2</sub>Zr<sub>2</sub>O<sub>7</sub> and Li<sub>2</sub>MnO<sub>3</sub> phases were undetectable at 900 °C.

Fig. 5a and b represented the XRD patterns and Raman spectra of sc-NMC631 + LLZTO composites sintered at various temperatures. No new phases were detected, suggesting potential thermal compatibility between sc-NMC631 and LLZTO up to 1000 °C. Fig. 5c summarizes the thermochemical stability of cathode materials in contact with LLZTO, which is highly dependent on their chemical composition and crystal structure. The sc-NMC631 showed the greatest thermochemical stability with LLZTO, with no evidence of secondary phase formation up to 1000 °C. In contrast, pc-LCO exhibited interfacial reactions with LLZTO starting at 700 °C, leading to the formation of La<sub>2</sub>Zr<sub>2</sub>O<sub>7</sub> and LaCoO<sub>3</sub>, both of which are ionically and electronically insulating phases that can impede Li-ion transport across the interface. For pc-NMC cathodes, the onset temperature for side reactions with LLZTO varied with composition. pc-NMC811, with the highest Ni content, exhibited reactivity as low as 500 °C, while pc-NMC631, 532, 111 remained stable up to 600 °C. All pc-NMC samples formed LaMO<sub>3</sub> and La<sub>2</sub>Zr<sub>2</sub>O<sub>7</sub> secondary phases; but La<sub>2</sub>(Ni<sub>0.5</sub>Li<sub>0.5</sub>)O<sub>4</sub> was detected only in high-Ni-content samples (NMC811, 631, 532), and Li<sub>2</sub>MnO<sub>3</sub> only appeared in Ni-lean NMC111. pc-LNMO begins reacting with LLZTO at 400 °C. Overall, these results demonstrate that the extent and nature of side reactions

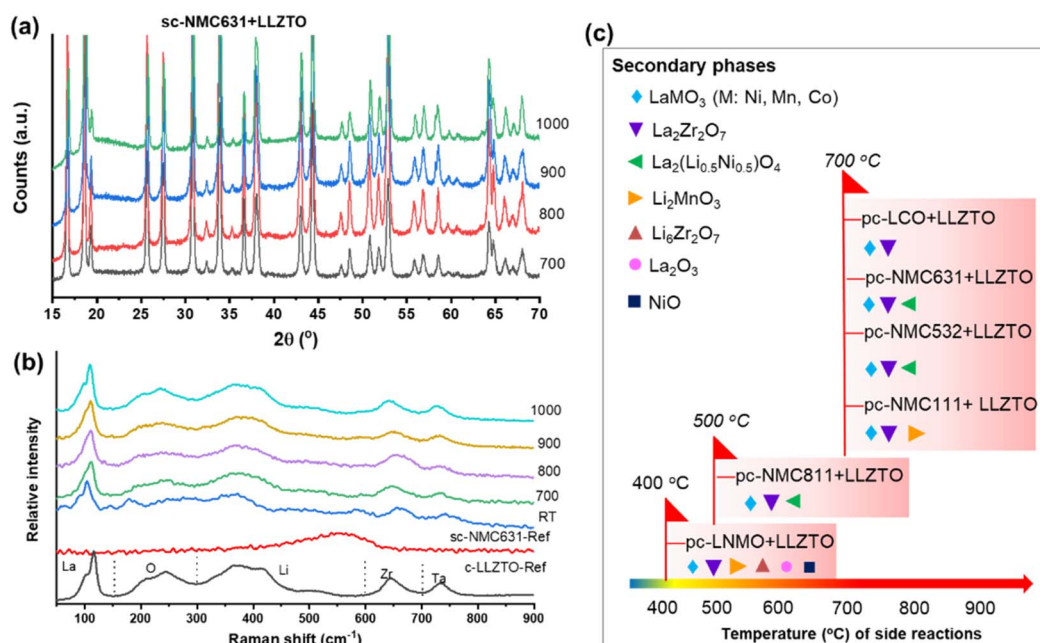


Fig. 5 XRD patterns and Raman spectra of (a and b) sc-NMC631 + LLZTO composites sintered at various temperatures in an O<sub>2</sub> atmosphere for 2 hours. (c) Comparison of onset temperatures for side reactions and secondary phase formation across different cathode + LLZTO systems.

depend on both the cathode composition and sintering temperature.

Single-crystalline NMC materials, including NMC532,<sup>21</sup>  $\text{LiNi}_{0.83}\text{Co}_{0.11}\text{Mn}_{0.06}\text{O}_2$ ,<sup>22</sup> and NMC811,<sup>32</sup> have been widely investigated in ASSLBs employing sulfide-based electrolytes. These systems benefit from the mechanical deformability and high processability of sulfide-based electrolytes, which eliminate the need for high-temperature sintering. In such systems, single-crystalline NMC cathodes offer enhanced structural integrity and superior cycling stability compared to their polycrystalline counterparts. To date, there have been no reported

studies on the electrochemical performance of single-crystalline cathodes when interfaced with LLZTO.

In this work, single-crystalline NMC631, chemically analogous to polycrystalline NMC631, was selected to evaluate the electrochemical performance of single-crystalline *versus* polycrystalline NMC cathodes in LLZTO-based ASSLBs. Cyclic voltammetry (CV) measurements in a half-cell configuration were performed to investigate the impact of high-temperature sintering and secondary phase formation on the electrochemical performance of both types of NMC631. The corresponding CV curves are presented in Fig. 6 and 7.

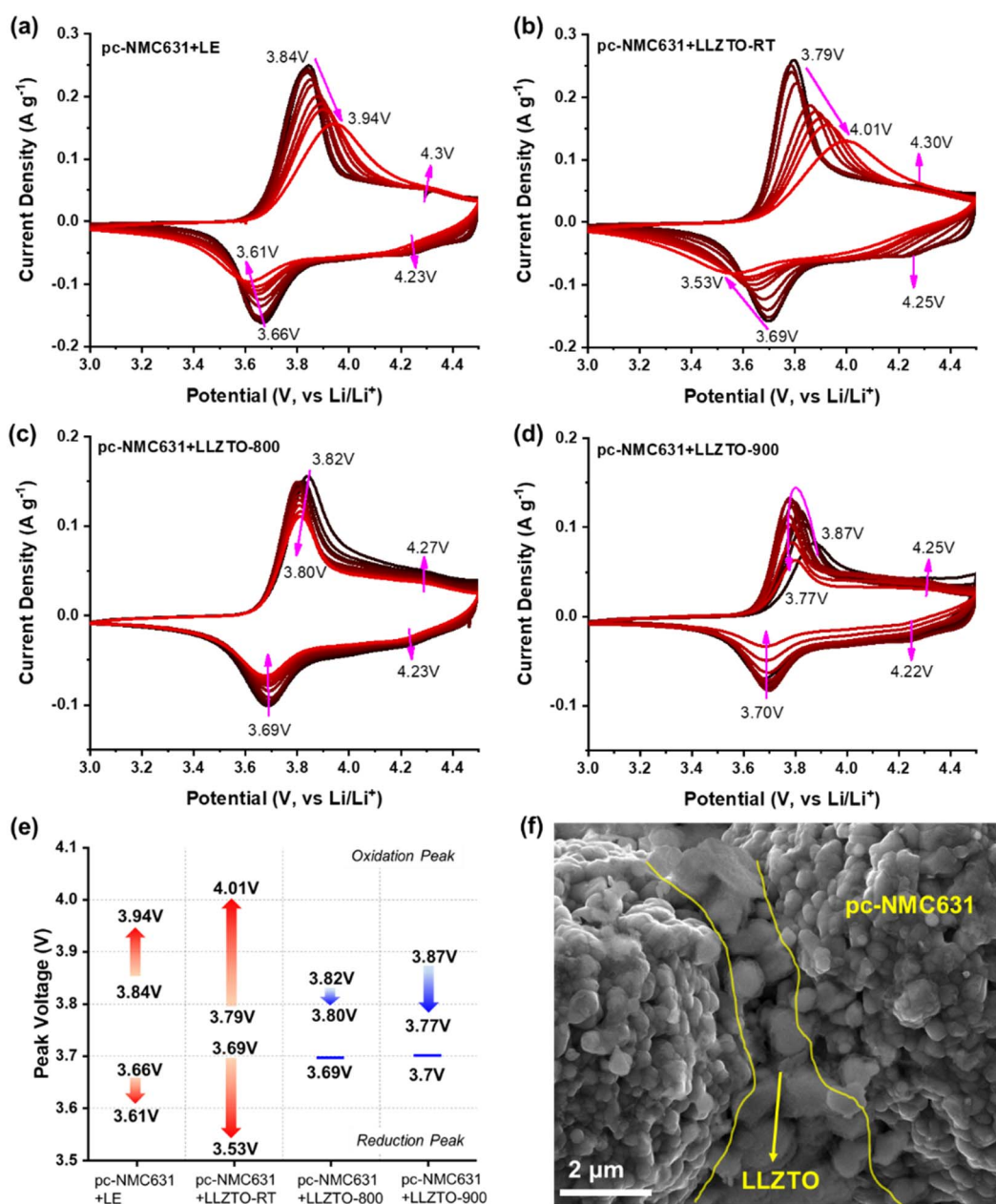


Fig. 6 CV curves from 2nd to 70th cycles within a potential window of 3.0–4.5 V (vs.  $\text{Li}^+/\text{Li}$ ) at a scan rate of  $0.1 \text{ mV s}^{-1}$ : (a) pc-NMC631 + LE, (b) pc-NMC631 + LLZTO-RT, (c) pc-NMC631 + LLZTO-800, and (d) pc-NMC631 + LLZTO-900, (e) comparison of voltage polarization near 3.8/3.7 V, (f) SEM image of pc-NMC631 + LLZTO-900 showing interfacial voids (highlighted with yellow lines).

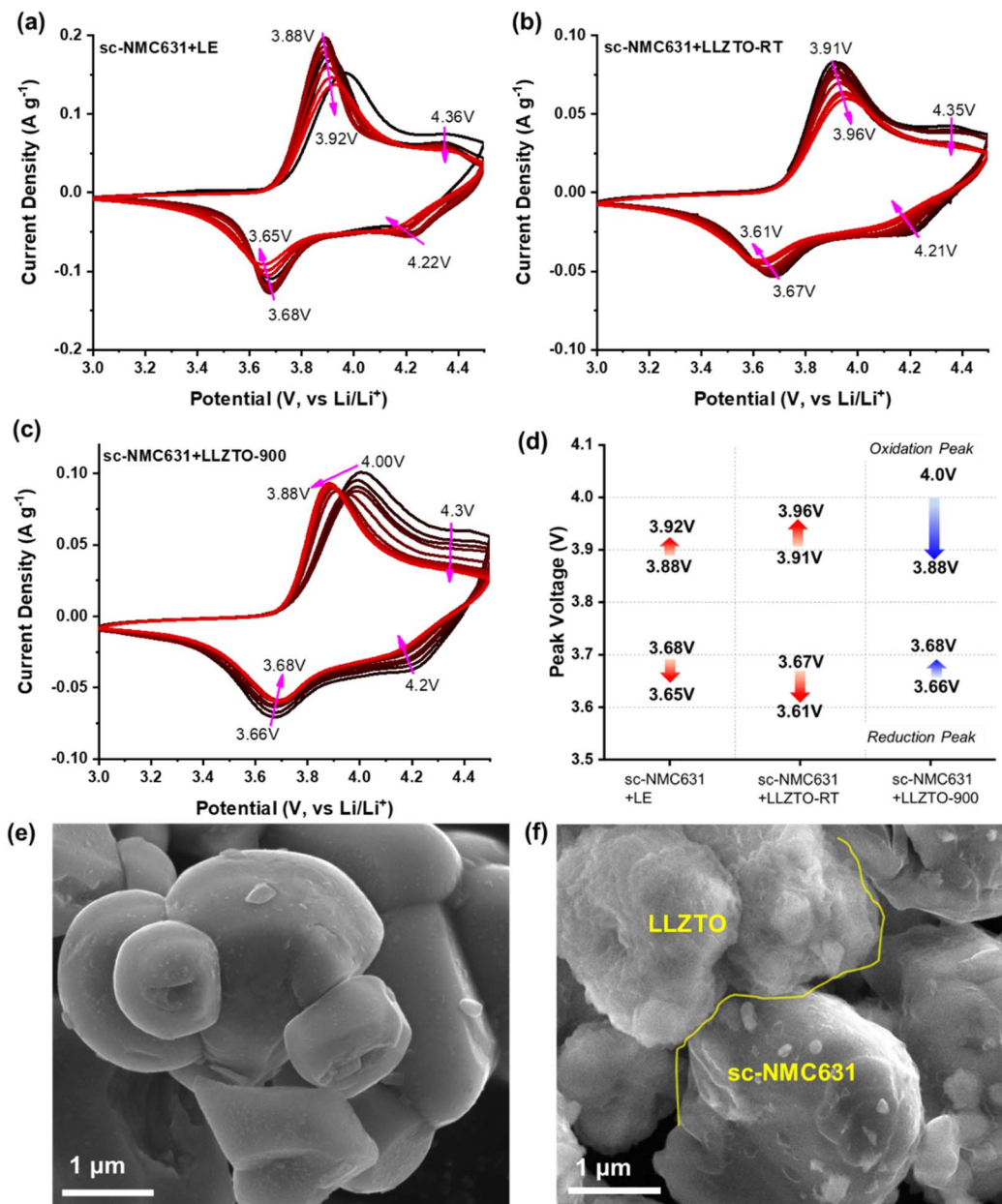


Fig. 7 CV curves from 2nd to 70th cycles within a potential window of 3.0–4.5 V (vs.  $\text{Li}^+/\text{Li}$ ) at a scan rate of  $0.1 \text{ mV s}^{-1}$  for (a) sc-NMC631 + LE, (b) sc-NMC631 + LLZTO-RT, and (c) sc-NMC631 + LLZTO-900. (d) Comparison of voltage polarization near 3.9/3.7 V. SEM images of (e) bare sc-NMC631 and (f) sc-NMC631 + LLZTO-900, with yellow line marking the interfaces.

The CV response of pc-NMC631 with a liquid electrolyte (LE) (Fig. 6a) serves as a reference for evaluating the electrochemical behavior of LLZTO-based composites. Fig. 6b–d compare the CV curves of pc-NMC631 + LLZTO composites sintered at room temperature (RT), 800 °C, and 900 °C. All samples exhibit distinct redox peaks near 3.8/3.7 V, corresponding to the reversible hexagonal-to-monoclinic ( $\text{H1} \leftrightarrow \text{M}$ ) phase transition during Li-ion extraction/insertion. This transition involves slight gliding of adjunct transition metal–oxygen (TM–O) layers. Additionally, broad redox peaks observed at  $\sim 4.3/4.2$  V are attributed to multiphase transitions ( $\text{M} \leftrightarrow \text{H2} \leftrightarrow \text{H3}$ ) during continued (de-)lithiation. This is a well-understood lithiation

processes.<sup>33</sup> Specifically, as Li ions are extracted from the M phase, the *c* lattice parameter expands, resulting in the H2 phase due to the increased repulsion between neighboring oxygen layers. Further Li-ion extraction leads to the H3 phase, characterized by gliding of TM–O layers toward adjacent Li planes. Notably, the high-temperature sintered composites (800 °C and 900 °C) exhibit lower voltage polarization and improved cycling stability compared to the non-sintered and LE-based cells, as shown in Fig. 6e. This improvement is attributed to enhanced crystallinity of NMC631 after thermal treatment. However, the high-temperature samples, also show reduced peak intensities in the CV curves, suggesting lower

specific capacity. This decline is likely due to inactive secondary phases (Fig. 4c and d) and increased resistance at solid–solid interfaces, which limits Li-ion transport. As observed in the SEM image of pc-NMC631 + LLZTO-900 (Fig. 6f), poor interfacial contact with voids, gaps, and localized point-to-point connections further hinders ion conduction and contributes to capacity loss. HR-TEM image (Fig. S7a†) shows a blur region between LLZTO and pc-NMC631 indicating the interfacial resistive phase.

The thermochemical stability of sc-NMC631 with LLZTO shown in Fig. 5, confirms the absence of secondary phase formation. Building on this, Fig. 7a–c illustrate the electrochemical behavior of sc-NMC631-based composites. All samples, including bare sc-NMC631, sc-NMC631 + LLZTO-RT, and sc-NMC631 + LLZTO-900, exhibit two pairs of redox peaks at  $\sim 3.9/3.7$  V and  $\sim 4.3/4.2$  V, corresponding to phase transitions during (de-)lithiation processes.<sup>33–35</sup> Among them, sc-NMC631 + LLZTO-900 demonstrates reduced polarization during cycling, whereas increased polarization is observed in non-sintered counterpart, as shown in Fig. 7d. Despite no secondary phases formed in sc-NMC631 + LLZTO-900, its current response is roughly 50% that of the bare sc-NMC631, indicating substantial capacity loss. This diminished performance likely arises from the misalign in Li-ion transport pathways between the single-crystalline NMC631 and polycrystalline LLZTO (Fig. S7b†), in addition to morphological discontinuities such as voids, interparticle gaps, limited point-to-point contacts

as observed in Fig. 7f. The coarse surface of LLZTO in Fig. 7f is attributed to the high-temperature calcination process.<sup>36,37</sup>

The rate capability and specific capacity of pc- and sc-NMC631 systems were evaluated at C-rates of 0.05C, 0.1C, 0.2C, 0.5C, and 1C. The theoretical capacities used for C-rate calculations were  $175 \text{ mAh g}^{-1}$  for pc-NMC631 and  $185 \text{ mAh g}^{-1}$  for sc-NMC631, with a voltage range of 3.0–4.3 V (vs.  $\text{Li}^+/\text{Li}$ ), as specified by the suppliers. To further assess structural stability under high charge potentials, an upper cutoff voltage of 4.5 V was employed.

Fig. 8 compares the rate performance of pc- and sc-NMC631 systems. The bare pc-NMC631 cathode (Fig. 8a) delivers discharge capacities of 200.5, 199.9, 191.5, 182.4, and 173.3  $\text{mAh g}^{-1}$  at 0.05C, 0.1C, 0.2C, 0.5C, and 1C, respectively. In contrast, pc-NMC631 + LLZTO-RT shows significantly lower capacities: 171.4, 160.4, 149.5, 128.5, and 103.3  $\text{mAh g}^{-1}$  at the same rates. High-temperature sintering further aggravates capacity degradation. Specifically, pc-NMC631 + LLZTO-800 and pc-NMC631 + LLZTO-900 exhibit 40% and 63% reductions in specific capacity at 0.1C, respectively, and the related discharge–charge curves are provided in Fig. 8c. These capacity reductions are primarily attributed to the formation of resistive interfacial phases such as  $\text{LaMO}_3$ , which hinder Li-ion transport.<sup>38</sup> The higher sintering temperatures accelerate new phase formation. In the pc-NMC631 + LLZTO-RT, capacity loss is attributed to poor interfacial contact and elevated charge transfer resistance, as depicted in Fig. 9a.

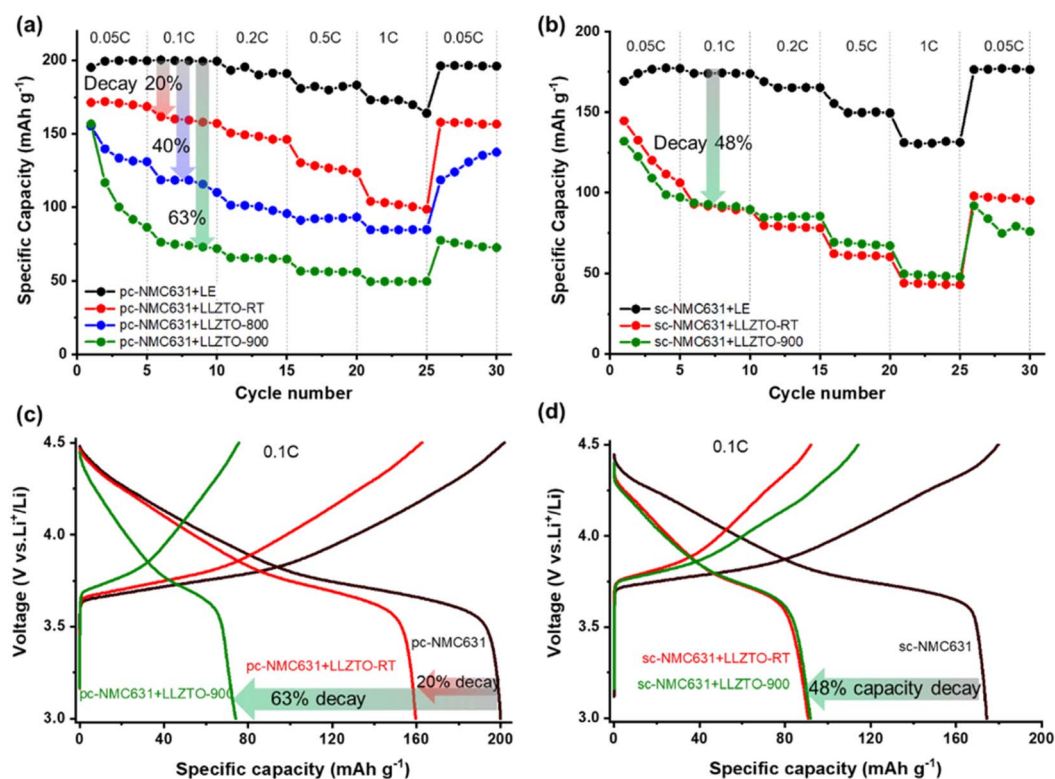


Fig. 8 Rate performance of (a) pc-NMC631 and (b) sc-NMC631 systems, showing discharge capacities. Representative discharge–charge curves for (c) pc-NMC631 and (d) sc-NMC631 at 0.1C.

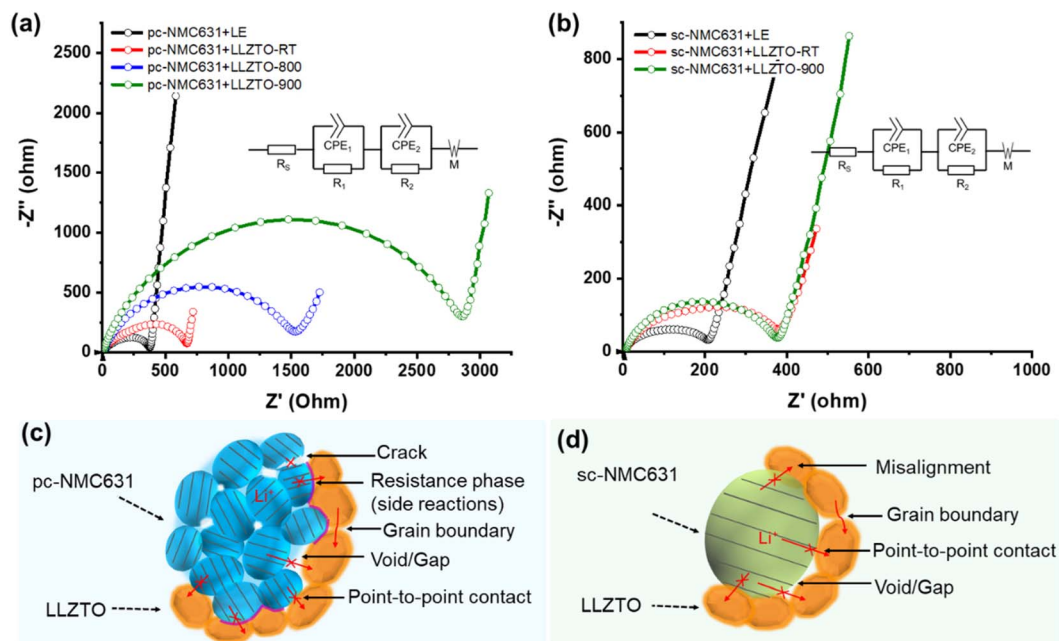


Fig. 9 Nyquist plots of (a) pc-NMC631 and (b) sc-NMC631 systems, with corresponding equivalent circuit models shown in the insets. Schematic diagrams illustrating Li-ion transport in (c) pc-NMC631 and (d) sc-NMC631 composite cathodes.

The bare sc-NMC631 cathode delivers discharge capacities of 175.4, 173.9, 165.1, 149.6, and 130.8 mAh g<sup>-1</sup> at 0.05C, 0.1C, 0.2C, 0.5C, and 1C, respectively. However, the incorporation of LLZTO results in ~48% capacity reduction at 0.1C, regardless of sintering treatment (Fig. 8b). The comparable performance between sc-NMC631 + LLZTO-900 and sc-NMC631 + LLZTO-RT is attributed to the high thermal stability of the sc-NMC631 with LLZTO and the lack of secondary phase formation. The capacity losses in these composites are therefore ascribed to mismatched Li-ion transport pathways between LLZTO and sc-NMC631, and inefficient solid–solid contact, which limits active site utilization. Despite no new phase formation, sc-NMC631 + LLZTO-900 exhibits lower Coulombic efficiency than sc-NMC631 + LLZTO-RT (Fig. 8d), possibly due to surface reconstruction or stoichiometric deviations induced by high-temperature treatment.

Electrochemical impedance spectroscopy (EIS) was employed to further investigate charge transfer behavior in the polycrystalline and single-crystalline NMC systems (Fig. 9). Both pc- and sc-NMC631 samples show increased charge transfer resistance upon LLZTO incorporation. In both cases, adding LLZTO (1 : 1 wt%) doubles the resistance, due to the lower ionic conductivity of LLZTO and interfacial discontinuities such as voids, interparticle gaps, and point-to-point contact, as confirmed by SEM (Fig. 6f and 7f). Among pc-NMC631 systems in Fig. 9a, pc-NMC631 + LLZTO-900 exhibits the highest charge transfer resistance, approximately twice that of pc-NMC631 + LLZTO-800, four times that of pc-NMC631 + LLZTO-RT, and eight times that of the bare pc-NMC631 electrode. This dramatic increase stems from the formation of interfacial resistive phases (e.g., LaMo<sub>3</sub> and La<sub>2</sub>(Ni<sub>0.5</sub>Li<sub>0.5</sub>)O<sub>4</sub>), as evidenced by Raman analysis (Fig. 4c and d), along with the worsened solid–solid

contact. These factors collectively result in a 40% capacity reduction in pc-NMC631 + LLZTO-800 and a 63% reduction in pc-NMC631 + LLZTO-900. In contrast, sc-NMC631 + LLZTO-900 (Fig. 9b) displays comparable charge transfer resistance to sc-NMC631 + LLZTO-RT, consistent with their similar capacity retention. This result underscores the benefit of improved thermal compatibility between sc-NMC631 and LLZTO, which mitigates the formation of interfacial phases. Nevertheless, the LLZTO incorporation still imposes a general increase in charge transfer resistance, thereby, limiting the electrochemical performance of both pc- and sc-NMC cathodes. These results highlight the critical role of interfacial engineering in mitigating charge transfer resistance and maximizing capacity in ASSLBs.

## 4. Conclusions

This study systematically investigated the thermochemical compatibility of various commercial cathode materials, including polycrystalline and single-crystalline, with cubic LLZTO under an O<sub>2</sub> atmosphere. The content of interfacial reactions and secondary phase formation was found to strongly depend on cathode composition, crystal structure, and sintering temperature. For pc-LCO + LLZTO composites, Li-deficient phases such as La<sub>2</sub>Zr<sub>2</sub>O<sub>7</sub> and LaCoO<sub>3</sub> emerged at 700–900 °C. pc-LNMO + LLZTO composites produced La<sub>2</sub>Zr<sub>2</sub>O<sub>7</sub> and Li<sub>2</sub>MnO<sub>3</sub> at 400 °C. In high-Ni content pc-NMC811, secondary phase formation began at 500 °C. pc-NMC631, 532, 111 exhibited thermochemical stability with LLZTO up to 600 °C. sc-NMC631 demonstrated the highest thermochemical stability with LLZTO, with no evidence of secondary phase formation up to 1000 °C. The electrochemical performance of pc- and sc-

NMC631 was further evaluated, as representative polycrystalline and single-crystalline systems. In pc-NMC631 composites, high-temperature sintering improved interfacial adhesion but resulted in further capacity losses due to resistive secondary phase formation, which blocked Li-ion transport. In contrast, sc-NMC631 systems, regardless of sintering, showed comparable charge transfer resistance and specific capacities, reflecting the thermal stability. Nevertheless, capacity remained limited due to misalignment of Li-ion transport pathways between the single-crystalline cathode and LLZTO. These findings emphasize the critical importance of interfacial stability between cathode and LLZTO under high-temperature processing. Minimizing secondary phase formation and optimizing charge transfer across solid–solid interfaces are essential strategies for enhancing performance of ASSLBs.

## Data availability

The authors confirm that the data supporting the findings of this study are available within the article and its ESI.†

## Author contributions

L. K. conceived the original concept and supervised the experiments. Z. M. contributed to the sintering experiments, characterization, and conducted electrochemical performance testing. G. L. contributed to the sintering experiments and conducted TGA testing. K. A. S. assisted with EIS simulation and analysis and contributed to Raman characterization. L. K. and Z. M. wrote the manuscript. L. K. and C. M. edited the manuscript.

## Conflicts of interest

The authors declare no conflict of interest.

## Acknowledgements

L. K. acknowledges funding support from the San Diego State University (SDSU) Startup Fund and SDSU Seed Grant. C. M. acknowledges funding support from the California Energy Commission, under contract number EPC-21-039 of which SDSU is a subrecipient through Solid Energies, Inc. who is the prime recipient. This work utilized the Electron Microscope Facility at SDSU. The authors also thank the Powder Technology Lab for access to the TA Instruments STD Q600, as well as the Department of Chemistry and Biochemistry at SDSU for access to Raman microscope.

## References

- 1 J. Janek and W. G. Zeier, Challenges in speeding up solid-state battery development, *Nat. Energy*, 2023, **8**, 230–240, DOI: [10.1038/s41560-023-01208-9](https://doi.org/10.1038/s41560-023-01208-9).
- 2 K. J. Kim, M. Balaish, M. Wadaguchi, L. Kong and J. L. M. Rupp, Solid-State Li-Metal Batteries: Challenges and Horizons of Oxide and Sulfide Solid Electrolytes and Their Interfaces, *Adv. Energy Mater.*, 2021, **11**, 2002689, DOI: [10.1002/aenm.202002689](https://doi.org/10.1002/aenm.202002689).
- 3 H. He, *et al.*, Interface Engineering on Constructing Physical and Chemical Stable Solid-State Electrolyte Toward Practical Lithium Batteries, *Energy Environ. Mater.*, 2024, **7**, e12699, DOI: [10.1002/eeem.12699](https://doi.org/10.1002/eeem.12699).
- 4 Y. Zhang, F. Chen, R. Tu, Q. Shen and L. Zhang, Field assisted sintering of dense Al-substituted cubic phase  $\text{Li}_7\text{La}_3\text{Zr}_2\text{O}_{12}$  solid electrolytes, *J. Power Sources*, 2014, **268**, 960–964, DOI: [10.1016/j.jpowsour.2014.03.148](https://doi.org/10.1016/j.jpowsour.2014.03.148).
- 5 X. Han, *et al.*, Negating interfacial impedance in garnet-based solid-state Li metal batteries, *Nat. Mater.*, 2017, **16**, 572–579, DOI: [10.1038/nmat4821](https://doi.org/10.1038/nmat4821).
- 6 L. J. Miara, W. D. Richards, Y. E. Wang and G. Ceder, First-Principles Studies on Cation Dopants and Electrolyte|Cathode Interphases for Lithium Garnets, *Chem. Mater.*, 2015, **27**, 4040–4047, DOI: [10.1021/acs.chemmater.5b01023](https://doi.org/10.1021/acs.chemmater.5b01023).
- 7 T. Deng, *et al.*, Tuning the Anode–Electrolyte Interface Chemistry for Garnet-Based Solid-State Li Metal Batteries, *Adv. Mater.*, 2020, **32**, 2000030, DOI: [10.1002/adma.202000030](https://doi.org/10.1002/adma.202000030).
- 8 H. He, *et al.*, Enabling interfacially compatible and high-voltage-tolerant lithium metal batteries with gradient composited solid-state electrolytes, *J. Mater. Chem. A*, 2024, **12**, 22971–22980, DOI: [10.1039/D4TA03587A](https://doi.org/10.1039/D4TA03587A).
- 9 K. Park, *et al.*, Electrochemical Nature of the Cathode Interface for a Solid-State Lithium-Ion Battery: Interface between  $\text{LiCoO}_2$  and Garnet- $\text{Li}_7\text{La}_3\text{Zr}_2\text{O}_{12}$ , *Chem. Mater.*, 2016, **28**, 8051–8059, DOI: [10.1021/acs.chemmater.6b03870](https://doi.org/10.1021/acs.chemmater.6b03870).
- 10 L. Zhao, *et al.*, Constructing Low-Impedance  $\text{Li}_7\text{La}_3\text{Zr}_2\text{O}_{12}$ -Based Composite Cathode Interface for All-Solid-State Lithium Batteries, *Small Struct.*, 2022, **3**, 2200200, DOI: [10.1002/sstr.202200200](https://doi.org/10.1002/sstr.202200200).
- 11 Y. Ren, T. Liu, Y. Shen, Y. Lin and C. W. Nan, Chemical compatibility between garnet-like solid state electrolyte  $\text{Li}_{6.75}\text{La}_3\text{Zr}_{1.75}\text{Ta}_{0.25}\text{O}_{12}$  and major commercial lithium battery cathode materials, *J. Materiomics*, 2016, **2**, 256–264, DOI: [10.1016/j.jmat.2016.04.003](https://doi.org/10.1016/j.jmat.2016.04.003).
- 12 C.-Y. Yu, J. Choi, J. Han, E. Lee and J.-H. Kim, Phase Stability of Garnet Solid-Electrolyte Interfacing with Various Cathodes in All Solid-State Batteries, *J. Electrochem. Soc.*, 2022, **169**, 020520, DOI: [10.1149/1945-7111/ac4e5b](https://doi.org/10.1149/1945-7111/ac4e5b).
- 13 B. Gotzen, *et al.*, Cathode-electrolyte material interactions during manufacturing of inorganic solid-state lithium batteries, *J. Electroceram.*, 2016, **38**, 197–206, DOI: [10.1007/s10832-016-0062-x](https://doi.org/10.1007/s10832-016-0062-x).
- 14 G. Vardar, *et al.*, Structure, Chemistry, and Charge Transfer Resistance of the Interface between  $\text{Li}_7\text{La}_3\text{Zr}_2\text{O}_{12}$  Electrolyte and  $\text{LiCoO}_2$  Cathode, *Chem. Mater.*, 2018, **30**, 6259–6276, DOI: [10.1021/acs.chemmater.8b01713](https://doi.org/10.1021/acs.chemmater.8b01713).
- 15 K. H. Kim, *et al.*, Characterization of the interface between  $\text{LiCoO}_2$  and  $\text{Li}_7\text{La}_3\text{Zr}_2\text{O}_{12}$  in an all-solid-state rechargeable lithium battery, *J. Power Sources*, 2011, **196**, 764–767, DOI: [10.1016/j.jpowsour.2010.07.073](https://doi.org/10.1016/j.jpowsour.2010.07.073).
- 16 L. Miara, *et al.*, About the Compatibility between High Voltage Spinel Cathode Materials and Solid Oxide

- Electrolytes as a Function of Temperature, *ACS Appl. Mater. Interfaces*, 2016, **8**, 26842–26850, DOI: [10.1021/acsami.6b09059](https://doi.org/10.1021/acsami.6b09059).
- 17 C. Roitzheim, *et al.*, All-Solid-State Li Batteries with NCM-Garnet-Based Composite Cathodes: The Impact of NCM Composition on Material Compatibility, *ACS Appl. Energy Mater.*, 2022, **5**, 6913–6926, DOI: [10.1021/acsami.2c00533](https://doi.org/10.1021/acsami.2c00533).
  - 18 A. Bauer, *et al.*, Impact of Ni-Mn-Co-Al-Based Cathode Material Composition on the Sintering with Garnet Solid Electrolytes for All-Solid-State Batteries, *ACS Appl. Energy Mater.*, 2022, **5**, 6913–6926, DOI: [10.1021/acs.chemmater.3c01573](https://doi.org/10.1021/acs.chemmater.3c01573).
  - 19 S. Hong, *et al.*, Structural and Chemical Compatibilities of  $\text{Li}_{1-x}\text{Ni}_{0.5}\text{Co}_{0.2}\text{Mn}_{0.3}\text{O}_2$  Cathode Material with Garnet-Type Solid Electrolyte for All-Solid-State Batteries, *Small*, 2021, **17**, 2103306, DOI: [10.1002/smll.202103306](https://doi.org/10.1002/smll.202103306).
  - 20 B. Zahiri, *et al.*, Revealing the role of the cathode-electrolyte interface on solid-state batteries, *Nat. Mater.*, 2021, **20**, 1392–1400, DOI: [10.1038/s41563-021-01016-0](https://doi.org/10.1038/s41563-021-01016-0).
  - 21 C. Wang, *et al.*, Single crystal cathodes enabling high-performance all-solid-state lithium-ion batteries, *Energy Storage Mater.*, 2020, **30**, 98–103, DOI: [10.1016/j.ensm.2020.05.007](https://doi.org/10.1016/j.ensm.2020.05.007).
  - 22 W. Jiang, *et al.*, Well-dispersed single-crystalline nickel-rich cathode for long-life high-voltage all-solid-state batteries, *J. Power Sources*, 2021, **508**, 230335, DOI: [10.1016/j.jpowsour.2021.230335](https://doi.org/10.1016/j.jpowsour.2021.230335).
  - 23 E. Trevisanello, R. Ruess, G. Conforto, F. H. Richter and J. Janek, Polycrystalline and Single Crystalline NCM Cathode Materials—Quantifying Particle Cracking, Active Surface Area, and Lithium Diffusion, *Adv. Energy Mater.*, 2021, **11**, 2003400, DOI: [10.1002/aenm.202003400](https://doi.org/10.1002/aenm.202003400).
  - 24 K. Hara, T. Yano, K. Suzuki, *et al.*, Raman Imaging Analysis of Local Crystal Structures in  $\text{LiCoO}_2$  Thin Films Calcined at Different Temperatures, *Anal. Sci.*, 2017, **33**, 853–858, DOI: [10.2116/analsci.33.853](https://doi.org/10.2116/analsci.33.853).
  - 25 Q. Zhong, A. Bonakdarpour, M. Zhang, Y. Gao and J. R. Dahn, Synthesis and Electrochemistry of  $\text{LiNi}_x\text{Mn}_{2-x}\text{O}_4$ , *J. Electrochem. Soc.*, 1997, **144**, 205, DOI: [10.1149/1.1837386](https://doi.org/10.1149/1.1837386).
  - 26 J. Zheng, *et al.*, Tuning of Thermal Stability in Layered  $\text{Li}(\text{Ni}_x\text{Mn}_y\text{Co}_z)\text{O}_2$ , *J. Am. Chem. Soc.*, 2016, **138**, 13326–13334, DOI: [10.1021/jacs.6b07771](https://doi.org/10.1021/jacs.6b07771).
  - 27 G. Larraz, A. Orera and M. L. Sanjuán, Cubic phases of garnet-type  $\text{Li}_7\text{La}_3\text{Zr}_2\text{O}_{12}$ : The role of hydration, *J. Mater. Chem. A*, 2013, **1**, 11419–11428, DOI: [10.1039/c3ta11996c](https://doi.org/10.1039/c3ta11996c).
  - 28 A. M. Nolan, E. D. Wachsman and Y. Mo, Computation-guided discovery of coating materials to stabilize the interface between lithium garnet solid electrolyte and high-energy cathodes for all-solid-state lithium batteries, *Energy Storage Mater.*, 2021, **41**, 571–580, DOI: [10.1016/j.ensm.2021.06.027](https://doi.org/10.1016/j.ensm.2021.06.027).
  - 29 S. Han, *et al.*, A Full Oxide-Based Solid-State Lithium Battery and Its Unexpected Cathode Degradation Mechanism, *ACS Energy Lett.*, 2023, **8**, 4794–4805, DOI: [10.1021/acscenergylett.3c01759](https://doi.org/10.1021/acscenergylett.3c01759).
  - 30 W. S. Scheld, *et al.*, Rapid thermal processing of garnet-based composite cathodes, *J. Power Sources*, 2022, **545**, 231872, DOI: [10.1016/j.jpowsour.2022.231872](https://doi.org/10.1016/j.jpowsour.2022.231872).
  - 31 A. Yasmin, *et al.*,  $\text{La}_4\text{NiLiO}_8$ -Shielded Layered Cathode Materials for Emerging High-Performance Safe Batteries, *ACS Appl. Mater. Interfaces*, 2020, **12**, 826–835, DOI: [10.1021/acsami.9b18586](https://doi.org/10.1021/acsami.9b18586).
  - 32 X. Liu, *et al.*, Constructing a High-Energy and Durable Single-Crystal NCM811 Cathode for All-Solid-State Batteries by a Surface Engineering Strategy, *ACS Appl. Mater. Interfaces*, 2021, **13**, 41669–41679, DOI: [10.1021/acsami.1c11419](https://doi.org/10.1021/acsami.1c11419).
  - 33 X. Wang, H. Zhou, Z. Chen and X. Meng, Synchrotron-based X-ray diffraction and absorption spectroscopy studies on layered  $\text{LiNi}_x\text{Mn}_y\text{Co}_z\text{O}_2$  cathode materials: A review, *Energy Storage Mater.*, 2022, **49**, 181–208, DOI: [10.1016/j.ensm.2022.04.012](https://doi.org/10.1016/j.ensm.2022.04.012).
  - 34 Z. Ahaliabadeh, *et al.*, Understanding the Stabilizing Effects of Nanoscale Metal Oxide and Li-Metal Oxide Coatings on Lithium-Ion Battery Positive Electrode Materials, *ACS Appl. Mater. Interfaces*, 2021, **13**, 42773–42790, DOI: [10.1021/acsami.1c11165](https://doi.org/10.1021/acsami.1c11165).
  - 35 Y. Ruan, X. Song, Y. Fu, C. Song and V. Battaglia, Structural evolution and capacity degradation mechanism of  $\text{LiNi}_{0.6}\text{Mn}_{0.2}\text{Co}_{0.2}\text{O}_2$  cathode materials, *J. Power Sources*, 2018, **400**, 539–548, DOI: [10.1016/j.jpowsour.2018.08.056](https://doi.org/10.1016/j.jpowsour.2018.08.056).
  - 36 J. Tang, Y. Zhou, X. Li, X. Huang, W. Tang and B. Tian, In-situ  $\text{Li}_2\text{O}$ -atmosphere assisted solvent-free route to produce highly conductive  $\text{Li}_7\text{La}_3\text{Zr}_2\text{O}_{12}$  solid electrolyte, *Energy Mater.*, 2024, **4**, 400022, DOI: [10.20517/energymater.2023.87](https://doi.org/10.20517/energymater.2023.87).
  - 37 J. Qu, X. Duan, K. Xue and S. An, Preparation and Electrochemical Characteristics of the Co-Doped  $\text{Li}_7\text{La}_3\text{Zr}_2\text{O}_{12}$  Solid Electrolyte with  $\text{Fe}^{3+}$  and  $\text{Bi}^{3+}$ , *Molecules*, 2025, **30**, 2028, DOI: [10.3390/molecules30092028](https://doi.org/10.3390/molecules30092028).
  - 38 L. Cui, *et al.*, A cathode homogenization strategy for enabling long-cycle-life all-solid-state lithium batteries, *Nat. Energy*, 2024, **9**, 1084–1094, DOI: [10.1038/s41560-024-01596-6](https://doi.org/10.1038/s41560-024-01596-6).